The Aeronautical Journal (2025), 1–12
doi:10.1017/aer.2025.45

ROYAL AERONAUTICAL SOCIETY

RESEARCH ARTICLE

Phase-changing droplet dynamics in idealised trailing vortex flows

O. Avni and Y. Dagan

Faculty of Aerospace Engineering, Technion – Israel Institute of Technology, Haifa, Israel
Corresponding author: Y. Dagan; Email: yuvalda@technion.ac.il

Received: 14 September 2024; **Revised:** 27 February 2025; **Accepted:** 22 April 2025

Keywords: trailing vortex; droplet dynamics; phase-change

Abstract

This study investigates the dynamics of water droplets within a Batchelor vortex. Such an analytically described flow structure serves here as a model that may capture the essence of a trailing vortex. A Lagrangian approach is used to analyse the coupling between droplet motion and the flow field generated by the vortex. Under certain thermodynamic and hydrodynamic conditions, droplets may undergo evaporation and condensation when circulating the vortex core due to sharp changes in the environmental conditions induced by the vortex. The vortex-induced pressure drop is quantified using a non-dimensional vortex Euler number, revealing conditions required for condensation initiation within the vortex core. The onset of condensation is characterised by defining a mass transfer coefficient, indicating the direction and extent of mass transfer to the droplets. Our study uncovered a distinct clustering phenomenon linked to the initial Stokes number, with droplets showing a tendency to aggregate at higher Stokes numbers. The presented model may offer valuable insights into droplet dynamics within trailing vortices, contributing to improved modelling and prediction of droplet transport phenomena near trailing vortices.

Nomenclature

Roman symbols

c	chord length
$c_{p,f}$	carrier fluid heat capacity
$c_{p,p}$	droplet heat capacity
C_D	drag coefficient
C_m	mass transfer coefficient
d_0	initial droplet diameter
d_p	droplet diameter
D	drag
Eu_v	vortex Euler number
k_f	thermal conductivity of fluid
L	latent heat of vapourisation
p_0	far-field pressure
p_f	local fluid pressure
p_{sat}	vapour saturation pressure
$p_{v,p}$	partial vapour pressure at the particle interface
$p_{v,\infty}$	ambient partial vapour pressure
Pr	Prandtl number
r	radial distance from the wingtip vortex axis
R_{cond}	condensation core radius
Re_c	chord-based Reynolds number
Re_p	particle-based Reynolds number

S	vortex swirl number
Sc	Schmidt number
Ste_0^*	modified Stefan number
Stk_0	droplet initial Stokes number
t	time
T_0	far-field temperature
T_f	local fluid temperature
T_p	droplet temperature
T_{sat}	vapour saturation temperature
U	flight velocity
u_f	local flow velocity
u_p	droplet velocity
x_p	droplet spatial location
z	downstream distance from the wing

Greek symbols

Γ	initial vortex intensity
η	normalised radial position ($r^2/4z$)
θ	normalised temperature
ν_f	fluid kinematic viscosity
ρ_f	fluid density
ρ_p	droplet density
$\rho^*_{v,\infty}$	vapour ideal gas density in ambient conditions
τ_f	free-stream flow time scale
$\tau_{p,0}$	droplet's initial relaxation time
ϕ	relative humidity

1.0 Introduction

While the interactions between droplets and their environment are a fundamental problem in fluid mechanics [1, 2], our understanding of such phenomena is incomplete. The complexity of the general problem arises from the strong coupling between the carrier flow and the transport of mass, momentum and heat to the droplet, thus limiting the scope of any general analysis. Past studies have investigated the two-way coupling between simple vortices and droplets with a comparable length scale and found that these vortical structures could significantly alter the droplet evaporation rate in spray combustion systems [3–8]. Vortical structures might also completely change the dynamics and thermal behaviour of the single droplet [9–13].

A clear manifestation of such complex interactions is wingtip trailing vortices, which enhance the condensation and freezing of the air's vapour content and contribute to the formation of condensation trails. The resultant multiphase flow structures might alter the local radiative forcing and the photochemistry of the atmosphere [14]. The interaction between trailing vortices and dispersed particles may also influence the efficiency of aerial agricultural spraying, as the aircraft wake can alter the motion of the spray drops [15]. The analysis of multiphase trailing vortices using high-fidelity simulations may require the implementation of Lagrangian particle tracking. However, incorporating a detailed model might have high computational costs, even for relatively simple setups. Notably, Sölch and Kärcher [16, 17] used a Lagrangian particle tracking model in conjunction with high-fidelity LES simulations to investigate the dynamics of ice particles in vortex flows, with a focus on aerosol and ice microphysics in contrail formation. While their study primarily addresses the nucleation and growth of ice particles in moist air within trailing vortices, our work centres on the evaporation and condensation of liquid droplets in these vortices, which occur at lower altitudes, typically during takeoff, landing, or sharp manoeuvers [18, 19]. Furthermore, even the wake of high-performance racecars can induce sufficient pressure gradients to cause droplet condensation within the rear wingtip vortices.

https://doi.org/10.1017/aer.2025.45 Published online by Cambridge University Press

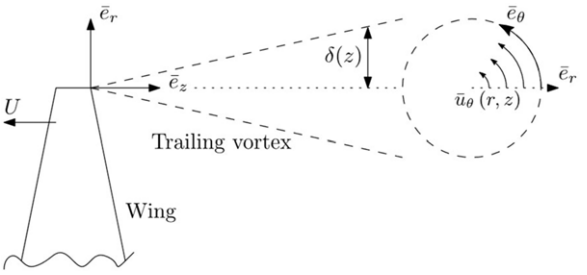

Figure 1. *Carrier flow setup.*

Therefore, this work offers a new Lagrangian analysis of the dynamics of droplets swirling within a simple, analytically described viscous vortical flow structure, the well-known Batchelor vortex. Batchelor [20] suggested such a similarity solution for modelling a trailing vortex far downstream from the wing itself owing to the complexity of such a three-dimensional unsteady problem [21].

Our analysis aims to reveal the complex interaction between Batchelor's Lamb-Oseen-based vortex and a Lagrangian droplet as it may undergo both evaporation and condensation due to sharp changes in the environmental conditions generated by the vortex. The nonlinear relations between the carrier flow fields, droplet relaxation time, drag forces, mass convection and heat exchange is derived and analysed. The isolation of the interaction between the modelled vortical flow and the droplets allows for a rudimentary, parametric investigation of the transport processes. Thus, the proposed model offers a new analytic tool that might aid in uncovering the underlying physical mechanisms governing the fundamental problem of droplet evaporation and condensation within wingtip trailing vortical structures.

2.0 Governing equations

The transport of discrete micron-sized droplets within a steady, analytically described Batchelor vortex is analysed here using a Lagrangian approach. The single droplet's spatial location $\boldsymbol{x}_p$, velocity $\boldsymbol{u}_p$, diameter d_p and temperature T_p are traced and coupled to the local flow $\boldsymbol{u}_f$, pressure p_f and temperature T_f fields. We assume the droplets are dispersed and dilute enough so that their motion does not affect the flow field; furthermore, any potential interactions between droplets are discounted. The equations for the carrier flow and the Lagrangian droplet are presented as follows.

2.1 Carrier flow

The investigated carrier flow, a three-dimensional Batchelor vortex, describes an axisymmetric vortical structure decaying due to viscous effects as illustrated by Fig. 1 flow. The initial vortex intensity Γ is determined by the wing's geometry and the flight conditions. The customary time variable t is replaced here by U and z, the flight velocity and downstream distance from the wing, correspondingly. Assuming the trailing vortex system is generated by a wing on which the total drag force is D, the velocity field of such flow may be expressed in cylindrical coordinates as

$$\tilde{\mathbf{u}}_f = \left[\frac{\Gamma}{2\pi\tilde{r}}\left(1-e^{-\frac{U\tilde{r}^2}{4\nu_f\tilde{z}}}\right)\right]\bar{e}_\theta + \left[U - \frac{D}{8\pi\rho_f\nu_f z}e^{-\frac{U\tilde{r}^2}{4\nu_f\tilde{z}}}\right]\bar{e}_z. \tag{1}$$

when considering that the axial and azimuthal velocities decay independently [20]. Since the Batchelor vortex is an exact solution of the Navier-Stokes equation, we may extract an analytic expression for the pressure field induced by the vortical flow. As we investigate the droplets' dynamics near a vortical structure, this model assumes that the pressure drop is induced only by the circulation, i.e. the pressure

https://doi.org/10.1017/aer.2025.45 Published online by Cambridge University Press

drop matches the pressure changes within a Lamb-Oseen vortex. The pressure term yields [21]

$$\tilde{p}_f = p_0 - \frac{\rho_f \Gamma^2}{8\pi^2 \tilde{r}^2}\left[\left(1 - e^{-\frac{U\tilde{r}^2}{4\nu_f \tilde{z}}}\right)^2 + \frac{U\tilde{r}^2}{2\nu_f \tilde{z}}\left(\mathrm{Ei}\left(\frac{U\tilde{r}^2}{4\nu_f \tilde{z}}\right) - \mathrm{Ei}\left(\frac{U\tilde{r}^2}{2\nu_f \tilde{z}}\right)\right)\right], \tag{2}$$

given that p_0 is the far-field pressure and $\mathrm{Ei}(x) = \int_{-x}^{\infty} e^{-\xi}/\xi d\xi$ is the tabulated exponential integral notation.

We set c, the wing's chord length as the characteristic radial length, U as the characteristic velocity, and introduce the dimensionless variables

$$r = \tilde{r}/c; \quad z = \tilde{z}/c\mathrm{Re}_c; \quad \eta = r^2/4z; \quad u = \tilde{u}/U; \quad p = \tilde{p}/p_0, \tag{3}$$

where $\mathrm{Re}_c = cU/\nu_f$. Hence, Equation (1) and Equation (2) may be written in a dimensionless form as

$$\boldsymbol{u}_f = \frac{S}{r}\left(1 - e^{-\eta}\right)\bar{e}_\theta + \left(1 - \frac{C_D e^{-\eta}}{16\pi z}\right)\bar{e}_z. \tag{4}$$

$$p_f = 1 - \frac{\mathrm{Eu}_v}{r^2}\left[\left(1 - e^{-\eta}\right)^2 + 2\eta(\mathrm{Ei}(\eta) - \mathrm{Ei}(2\eta))\right], \tag{5}$$

using three dimensionless parameters: the wing's drag coefficient

$$C_D = \frac{D}{\frac{1}{2}\rho_f U^2 c^2}, \tag{6}$$

the vortex swirl number

$$S = \frac{\Gamma}{2\pi c U}, \tag{7}$$

and the *vortex Euler number*

$$\mathrm{Eu}_v = \frac{\rho_f \Gamma^2}{8\pi^2 c^2 p_0} = \frac{\frac{1}{2}\rho_f U^2 S^2}{p_0}, \tag{8}$$

which signifies the ratio between the dynamic pressure drop and the total pressure.

Figure 2 pressure_drop demonstrates the relation between Eu_v and the pressure field around the idealised trailing vortex; an increase of Eu_v manifests in lower absolute pressures at the origin of the vortex. The derived pressure field is used hereafter to couple the Lagrangian droplet transport with the thermodynamic gradients induced by the vortical flow. We also consider the vortex to be adiabatic; hence, one may couple the temperature field within the vortical viscous core to the pressure field

$$\tilde{T}_f = T_0\left(\frac{\tilde{p}_f}{p_0}\right)^{2/7}. \tag{9}$$

The temperature field outside the droplet is crucial for finding the droplet temperature, as it is dictated by, among other mechanisms, heat diffusion to the droplet.

2.2 Lagrangian equations

Maxey and Riley [22] formulated the generalised equations of motion for small particles in nonuniform, unsteady flows; they considered both gravity, drag, virtual mass and the Basset 'history' force. This study concerns the motion of a small liquid droplet in a gaseous medium; the particle-medium density ratio is large, and the droplet's characteristic length is much smaller relative to the vortex viscous core size. Hence, we neglect the forces due to undisturbed flow, virtual mass, Faxen's drag correction, rotational inertia and particle history terms. Additionally, we do not account for gravity and assume a linear drag term; the influence of both on the droplet dynamics will be relaxed and examined in future studies.

https://doi.org/10.1017/aer.2025.45 Published online by Cambridge University Press

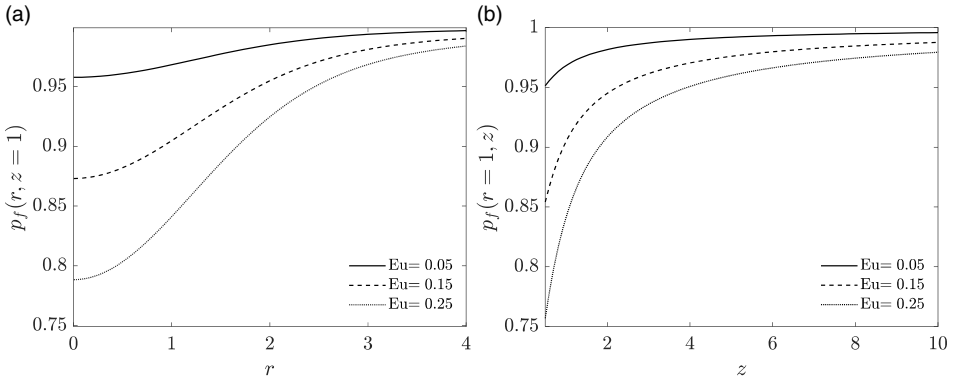

Figure 2. *Normalised pressure distribution $p_f(r, z)$ for various values of the non-dimensional Euler number Eu, as predicted by Equation (5). (a) Radial pressure distribution at axial location $z = 1$. (b) Pressure distribution along the vortex axis at radial location $r = 1$.*

We may now reduce the general form of the equations to the following:

$$\frac{d\mathbf{x_p}}{dt} = \mathbf{u_p}, \tag{10}$$

$$\frac{d\mathbf{u_p}}{dt} = \frac{\mathbf{u_f} - \mathbf{u_p}}{\mathrm{Stk}_0 d_p^2}, \tag{11}$$

where $\mathbf{x_p}$ and $\mathbf{u_p}$ are the droplet location and velocity vectors in the vortex frame of reference, respectively. d_p is the particle diameter normalised by its initial diameter d_0, and

$$\mathrm{Stk}_0 = \frac{\tau_{p,0}}{\tau_f} = \frac{U\rho_p d_0^2}{18\mu_f c} \tag{12}$$

is the *droplet initial Stokes number*: the ratio between the particle's initial relaxation time and free-stream flow time scale. While valid for low particle Reynolds numbers $\mathrm{Re}_p = \left|\mathbf{u_f} - \mathbf{u_p}\right| d_p/\nu_f$, the linear drag model offers a good approximation for the drag forces acting on small droplets as their velocity relative to the local flowfield is typically low [23].

The size of the Lagrangian particle is governed by heat and mass transfer processes. Kulmala [24, 25] formulated the diffusive mass transfer at the droplet-gas interface for a quasi-stationary case while assuming that the medium is an ideal gas, the droplet-gas interface is saturated and a zeroth-order mass fraction profiles around the droplet. Although droplet ventilation may enhance the mass transfer out of the droplet, we aim to isolate the role of mass diffusivity and consider it the primary transfer mechanism. In terms of droplet diameter, the dimensionless mass equation is

$$\frac{d\left(d_p^2\right)}{dt} = \frac{4\rho^*_{v,\infty}}{9\mathrm{ScStk}_0\rho_f}\ln\left(\frac{p_0 p_f - p_{v,p}}{p_0 p_f - p_{v,\infty}}\right); \tag{13}$$

Sc is the non-dimensional Schmidt number, $\rho^*_{v,\infty}$ is the vapour ideal gas density in ambient conditions, $p_{v,p}$ is partial vapour pressure at the particle interface, and $p_{v,\infty}$ is the ambient partial vapour pressure. The difference between the vapour partial pressure at the interface and the vapour partial pressure at the far field dictates the mass flux to and from the droplet. Thus, we shall estimate both by assuming the Lagrangian particle consists of pure liquid water and the gaseous media is an air-vapour mixture with a relative humidity of ϕ. The diffusive driving force reduces to a single dimensionless number, the normalised mass transfer coefficient C_m [12]; its generalised term is

$$\frac{p_0 p_f - p_{v,p}}{p_0 p_f - p_{v,\infty}} = 1 + \frac{\phi p_{sat}\left(T_0\right) - p_{sat}\left(\tilde{T}_p\right)}{p_0 p_f - \phi p_{sat}\left(T_0\right)} = 1 + C_m. \tag{14}$$

https://doi.org/10.1017/aer.2025.45 Published online by Cambridge University Press

T_0 is the far-field carrier fluid temperature, $\tilde{T}_p$ is the (dimensional) droplet temperature, and $p_{sat}(T)$ is the vapour saturation pressure at a given temperature. The mass transfer coefficient sign and value indicate the nature of the mass transfer: evaporation occurs when $C_m < 0$ and the droplet interface vapour pressure is higher than far-field pressure, condensation occurs for $C_m > 0$ and the far-field vapour pressure is higher than the droplet interface pressure. Generally, the mass flux is proportional to the transfer coefficient value $\dot{m} \propto |C_m|$.

The droplet temperature is regulated by heat conduction and convection to the carrier medium at the droplet surface, the sensible heat stored within it, and heat advection due to mass transport. One may derive [13] the normalised energy conservation equation for a single droplet, assuming a zeroth-order temperature profile around the droplet. First, we introduce the non-dimensional temperature

$$\theta = \frac{\tilde{T} - T_0}{T_{sat}\left(p_0\right) - T_0} = \frac{\tilde{T} - T_0}{\Delta T_0}, \tag{15}$$

where $T_{sat}\left(p_0\right)$ is the vapour saturation temperature at the ambient pressure. Now, the Lagrangian energy equation yields

$$\frac{d\theta_p}{dt} = \frac{2}{3d_p^2}\left[\mathrm{Ste}_0^* \frac{d\left(d_p^2\right)}{dt} + \frac{4c_{p,f}}{9\mathrm{PrStk}_0 c_{p,p}}\left(\theta_f\left(\mathbf{x_p}\right) - \theta_p\right)\right], \tag{16}$$

where $\theta_f\left(\bar{x}_p\right)$ is the normalised carrier temperature at the droplet location, $c_{p,f}$ is the carrier fluid heat capacity, $c_{p,p}$ is the droplet heat capacity and $\mathrm{Pr} = c_{p,f}\nu_f/\rho_f k_f$ is the dimensionless Prandtl number. We also introduce a *modified Stefan number*, defined here as the ratio between the droplet substance's latent heat of evaporation and sensible heat maxima

$$Ste_0^* = \frac{L}{c_{p,p}\Delta T_0}, \tag{17}$$

denoting the latent heat of vapourisation as L.

Both the thermodynamic conditions and the vortex properties may affect the mass transfer coefficient C_m field within it. The pressure drop due to the rotating flow may give rise to distinct condensation zones within the vortex core; the following section analyses the influence of the dynamics of Lagrangian water droplets in and around vortices sustaining such conditions.

3.0 Results

3.1 Condensation core

The interaction between ambient thermodynamic conditions and localised variations induced by the vortex dictates the behaviour of the mass transfer coefficient, potentially leading to a change in its sign near the vortex centre. Namely, given the right conditions, condensation initiates in the vortex viscous core – as exhibited in many natural phenomena and industrial applications. Figure 3 illuminates the relation between ambient properties and the evolving condensation core of the vortex. Near the wing, where z tends to 0, the condensation core reaches the maximal radial value. However, as the circulation decays along the vortex axis, a decrease in pressure drop occurs. Thus, the condensation core radius progressively shrinks, and eventually, far from the wing, the core disappears as expected.

The influence of air relative humidity is depicted in Fig. 3(a). Lower relative humidity leads to smaller condensation cores that decay rapidly along the vortex axis. Moreover, a nonlinear relation between the changes in the relative humidity and the core size emerges; the core size significantly increases and subsequently diverges as $\phi \to 1$. Figure 3(b) illustrates how the vortex Euler number, representing the ratio between ambient and dynamic pressures within the vortex, affects the behaviour of the condensation core. As expected, lower Euler values result in smaller cores. Notably, the values of the vortex Euler number are constrained by physical considerations. For instance, when $Eu > 0.25$, the pressure at the vortex centre $p_f(r = 0)$ drops below absolute zero, an impossible thermodynamic state in gases.

https://doi.org/10.1017/aer.2025.45 Published online by Cambridge University Press

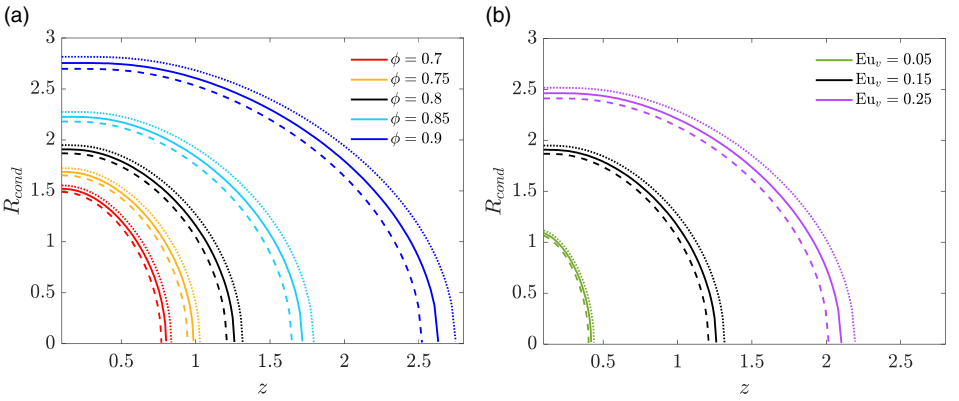

Figure 3. *Condensation core radius* $\mathrm{R_{cond}}$ *along the vortex axis for different vortex Euler numbers, relative humidities and ambient temperatures. (a) Constant Euler number* $\mathrm{Eu_v} = 0.15$ *and varying relative humidities* ϕ*. (b) Constant air relative humidity* $\phi = 0.8$ *and varying vortex Euler numbers* $\mathrm{Eu_v}$*. Dashed lines denote results obtained for ambient temperature of* $\mathrm{T_0} = 290\mathrm{K}$*, while solid and dotted lines denote results obtained for* $\mathrm{T_0} = 280\mathrm{K}$ *and* $\mathrm{T_0} = 274\mathrm{K}$*, correspondingly.*

Realistically, the limit of physically possible trailing vortices is significantly lower. The effect of ambient temperatures in the range $T_0 = 274K - 290K$ is also explored and presented in Fig. 3. Smaller cores, corresponding to lower Eu_v or ϕ values, are less influenced by temperature changes. However, given larger cores, the ambient temperature impact becomes more pronounced, though still relatively minor compared to other parameters. However, the air relative humidity is strongly temperature-dependent, indirectly influencing the characteristics of the condensation core.

3.2 Droplet dynamics

The Lagrangian governing equations presented in Section 2.2 suggest that one may characterise the complete dynamic and thermal behaviour of a droplet in the vicinity of idealised trailing vortices in terms of four state variables $X_p = \left[\mathbf{x_p}, \mathbf{u_p}, \mathbf{d_p^2}, \theta_\mathbf{p}\right]$. The complex coupling between the external, vortex-induced forcing and the droplet's response gives rise to a nonlinear dynamic system,

$$\dot{X}_p = F\left(X_p, \dot{X}_p, \ldots\right). \tag{18}$$

While aiming to investigate the system's dynamic response, the nonlinear ODE system will be solved numerically using an adaptive time-stepping fourth-order Runge-Kutta scheme.

Since we seek to study the dynamics of water droplets within trailing vortices wherein condensation cores are forming, the air's thermodynamic properties are fixed at $p_0 = 1atm$, $T_0 = 280K$ and $\phi = 0.8$. Here we focus our discussion on the influence of the droplet's properties, i.e. initial location $\mathbf{x_{p,0}}$ and $\mathrm{Stk_0}$, and thus set the vortex flow properties to be constant: $\mathrm{Eu}_v = 0.15, S = 1, C_D = 0.05$. Furthermore, the droplet area will be limited to $d_p^2 \geq 0.1$; i.e., the droplet diameter is limited to 1% of its initial diameter. Droplets crossing these thresholds are eliminated from the simulation; the mass equation, Equation (13), cannot capture the droplet's complete drying without imposing an arbitrary threshold on the droplet's size.

Figure 4 illustrates selected results of the Lagrangian model for droplets with various initial Stokes numbers: (a-b) $\mathrm{Stk_0} = 0.1$, (c-d) $\mathrm{Stk_0} = 1$, and (e-f) $\mathrm{Stk_0} = 10$. In each case, 20 droplets are distributed along the x and y axes inside the condensation core at equal distances from each other, all placed at $z = 0.1$. An initial no-slip condition is assumed, as the droplet's initial velocity is set to be equal to the local flow velocity. Similarly, the droplets are considered to maintain thermal equilibrium with the surrounding air, $\theta_p\left(\mathbf{x_p}\right) = \theta_\mathbf{f}$. The initial Stokes number is determined by both the flow regime and droplet

https://doi.org/10.1017/aer.2025.45 Published online by Cambridge University Press

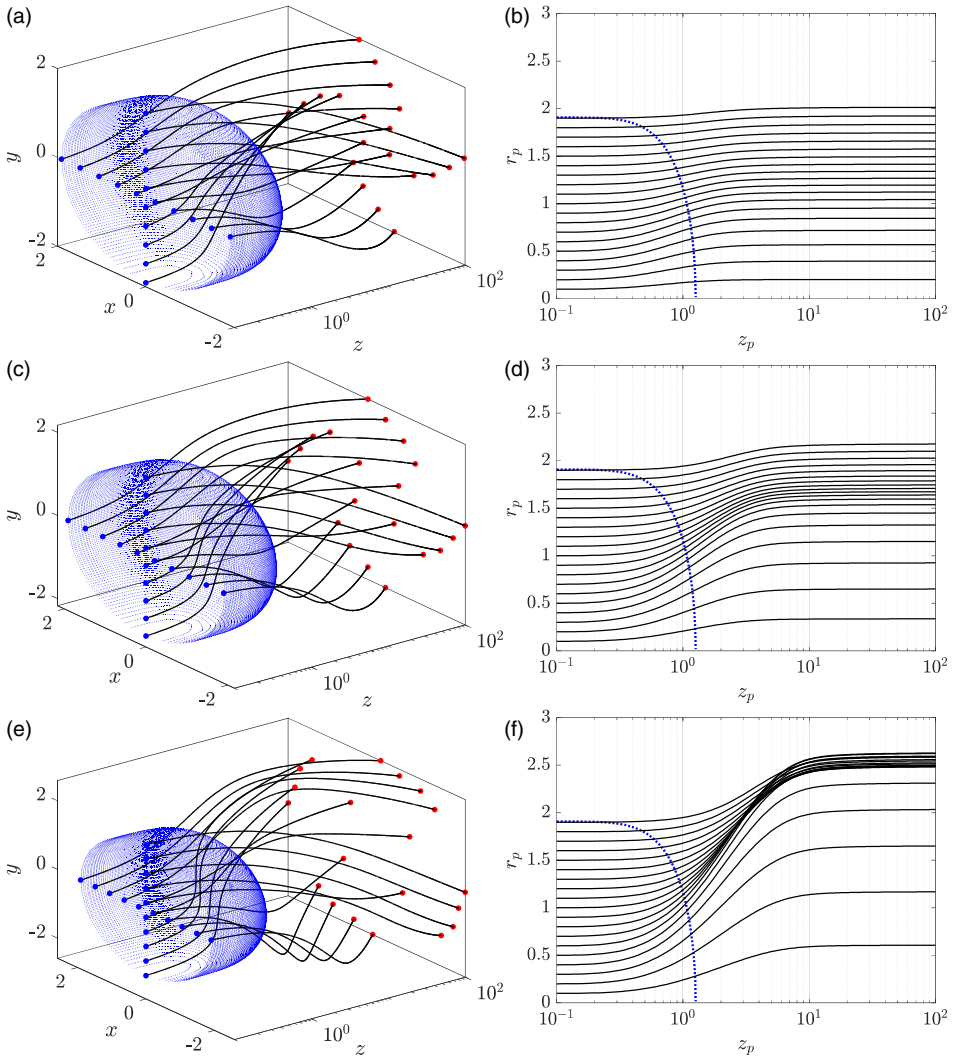

Figure 4. *Selected results of the Lagrangian model for droplets of various initial Stokes numbers: (a–b)* $\mathrm{Stk}_0 = 0.1$*, (c–d)* $\mathrm{Stk}_0 = 1$*, and (e–f)* $\mathrm{Stk}_0 = 10$*. The condensation core is illustrated by a blue ellipsoid, marking the edges of the region in which condensation occurs. The axial ordinate* z *is in a logarithmic scale. LHS panels (a),(c) and (e) present the three-dimensional trajectories of droplets placed at equal distances along* x *and* y *axes inside the condensation core. RHS panels (b),(d), and (f) present the radial location of the droplets as a function of their location along the vortex axis.*

size; the latter is dictated by the nucleation mechanism and is coupled to the thermodynamic conditions at nucleation inception. The present study does not aim to model the nucleation mechanisms of droplets from moist air, as its focus is on the growth and evaporation of pre-existing droplets within vortex flows.

For initial Stokes numbers below unity ($\mathrm{Stk}_0 < 1$), Fig. 4(a–b) reveals that the droplets retain scattered distribution without notable clustering. Their spread radius slightly exceeds the initial condensation core radius, indicating a relatively even dispersion throughout the vortex flow. However, clustering phenomena become more apparent as the initial Stokes number reaches unity ($\mathrm{Stk}_0 = 1$). Figure 4(d) highlight that this clustering primarily occurs when droplets exit the condensation core region, typically between $z = 1$ and $z = 5$. Beyond $z = 10$, the droplets' radial position stabilises as they steadily swirl within the vortex, ultimately undergoing complete evaporation. The initial growth by condensation, followed by

https://doi.org/10.1017/aer.2025.45 Published online by Cambridge University Press

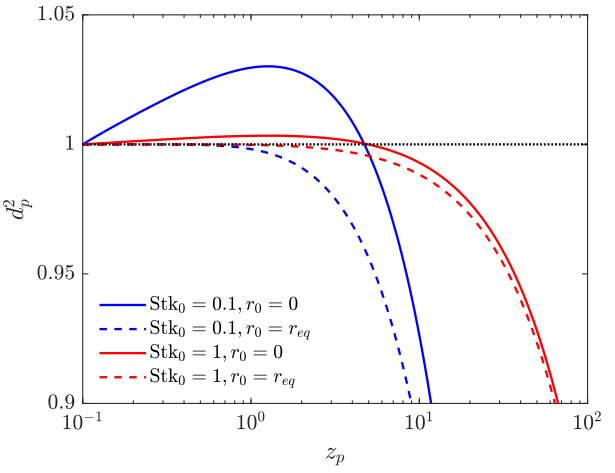

Figure 5. *Droplet square diameter as a function of its position along the vortex axis for two initial Stokes numbers,* $\mathrm{St}_0 = 0.1$ *and* 1. *Droplets are initially located either on the vortex axis* ($\mathrm{r}_0 = 0$) *or at the edge of the condensation core* ($\mathrm{r}_0 = \mathrm{r}_{\mathrm{eq}}$).

subsequent evaporation, is illustrated in Fig. 5, which shows the square diameter of four selected droplets. Two droplets are positioned just outside the vortex condensation core and thus undergo only evaporation. In contrast, droplets initially located on the vortex axis remain within it and initially grow in size. Once transported out of the condensation core, the mass transfer mechanism reverses, leading to evaporation at a rate similar to that of droplets initially outside the core. As expected, smaller droplets respond more sharply to thermodynamic conditions, both during the initial condensation phase and the subsequent evaporation phase.

With further increases in the initial Stokes number and surpassing $\mathrm{Stk}_0 > 1$, clustering of droplets emerges. Such droplets aggregate around specific radial locations, forming dense clusters with distinct spatial patterns. In the case of $\mathrm{Stk}_0 = 10$, Fig. 4(f) reveals that the clustering radius is expanding, surpassing the initial condensation core radius. The resulting pattern resembles an annular formation surrounding the core of the trailing vortex, with droplets accumulating around a specific radius.

Further investigation into the clustering phenomena was conducted through statistical analysis of 10^5 monodisperse droplets, as illustrated in Fig. 6. Initially, the particles were uniformly distributed across the cross-sectional area of the condensation core, simulating the aftermath of droplet nucleation. This simplified model aims to elucidate the underlying physical mechanisms governing droplet behaviour. The variability in droplet sizes is represented by different initial Stokes numbers.

For small droplets ($\mathrm{Stk}_0 \leq 0.1$), the radial probability density functions remain largely consistent across different axial positions. A slight decrease in droplet density near the axis is observed, attributable to centrifugal effects. As evident in Fig. 6(d), beyond $z > 10$, these small droplets begin to evaporate as the condensation core diminishes. The formation of annular structures becomes evident for $\mathrm{Stk}_0 \geq 1$. Figure 6(b) demonstrates this phenomenon, revealing a notable shift in the droplet location probability for $z \geq 5$, coinciding with the droplets' exit from the condensation region. For larger droplets ($\mathrm{Stk}_0 = 10$), this shift is more pronounced. The droplets aggregate within a relatively narrow radial band for $z \geq 5$, as shown in Fig. 6(c). The annular formation exhibits a slight radial expansion as the droplets evaporate far from the condensation region.

Figure 6(d) quantifies the mean droplet diameter variation as a function of axial position for different initial Stokes numbers, providing insight into the droplets' growth and evaporation patterns along their trajectories. These results suggest that a comprehensive analysis of droplet dynamics in such scenarios necessitates incorporating models accounting for droplet-droplet interactions, including collision,

https://doi.org/10.1017/aer.2025.45 Published online by Cambridge University Press

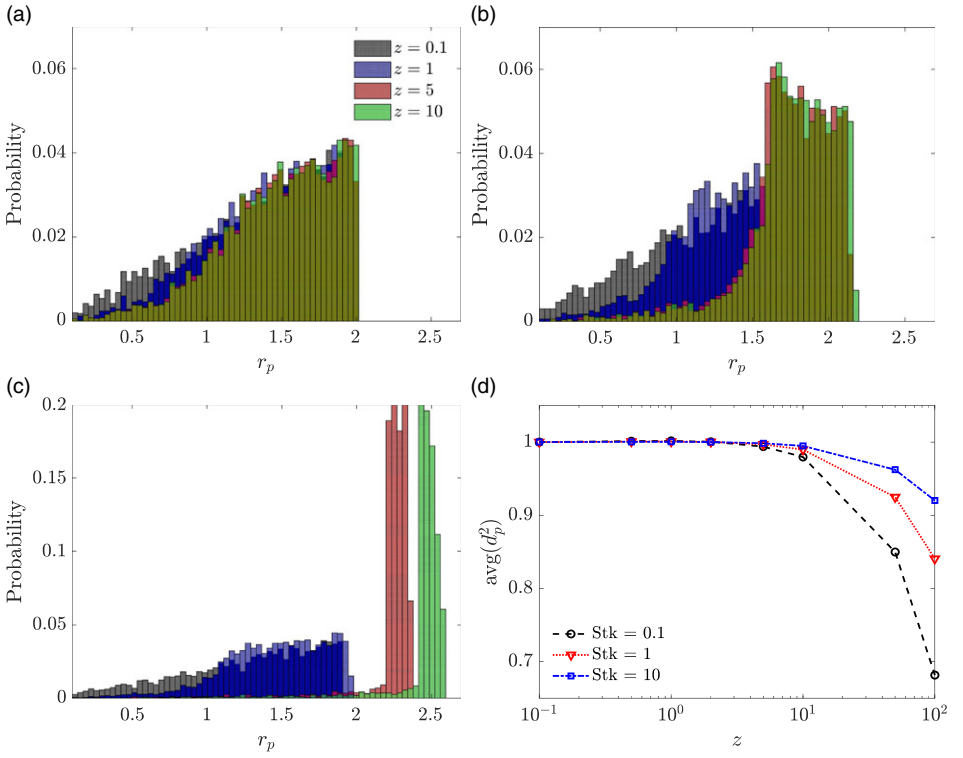

Figure 6. *Statistics from Lagrangian simulations of* 10^5 *monodispersed droplets. Droplets are initially randomly distributed within the condensation core at the axial plane* $\mathrm{z} = 0.1$. *(a–c) Radial probability density functions at axial positions* $\mathrm{z} = 0.1, 1, 5, 10$ *for droplets with initial Stokes numbers: (a)* $\mathrm{Stk}_0 = 0.1$, *(b)* $\mathrm{Stk}_0 = 1$, *and (c)* $\mathrm{Stk}_0 = 10$. *(d) Mean droplet diameter variation as a function of the axial location for different initial Stokes numbers.*

coalescence and grouping phenomena. The observed clustering behaviour indicates that the dispersed phase assumption may be invalid under certain conditions, particularly for larger droplets.

The onset of droplet evaporation as they are transported away from the condensation region was previously illustrated in Fig. 6(d). To further elucidate this phenomenon, we extended our simulations to determine the average axial location at which complete droplet evaporation occurs, effectively defining the length of the condensation trail. Figure 7 presents the trail length as a function of the initial droplet Stokes number (Stk_0) under various thermodynamic and flow conditions. As anticipated, smaller droplets (low Stk_0) evaporate rapidly, resulting in shorter trails. Generally, an increase in the initial Stokes number corresponds to an extension of the trail length.

The influence of thermodynamic states on trail length is significant. Figure 7(a) demonstrates that an increase in relative humidity (ϕ) suppresses evaporation, thereby extending the trail length across all Stk_0 values. Conversely, as shown in Fig. 7(b), the effect of changes in the relative pressure drop within the vortex is not linear. For small droplets ($\mathrm{Stk}_0 < 0.1$), an increase in Eu_v leads to a substantial elongation of the trail. However, for $\mathrm{Stk}_0 \parallel 0.1$, the trail length remains relatively unaffected by changes in Eu_v. This suggests that droplets with larger initial diameters are less influenced by condensation within the vortex core, as their initial size governs the dynamics. Interestingly, for low initial Stokes numbers $\mathrm{Stk}_0 \approx 10^{-4}$ combined with high $\mathrm{Eu}_v = 0.25$ values, a slight decline in trail length is observed. This behaviour may be attributed to enhanced entrapment of smaller droplets within the vortex. In such conditions, the droplets rapidly gain mass due to intense condensation inside the vortex core, altering their trajectory and thus extending their lifetime as compared with initially larger droplets.

https://doi.org/10.1017/aer.2025.45 Published online by Cambridge University Press

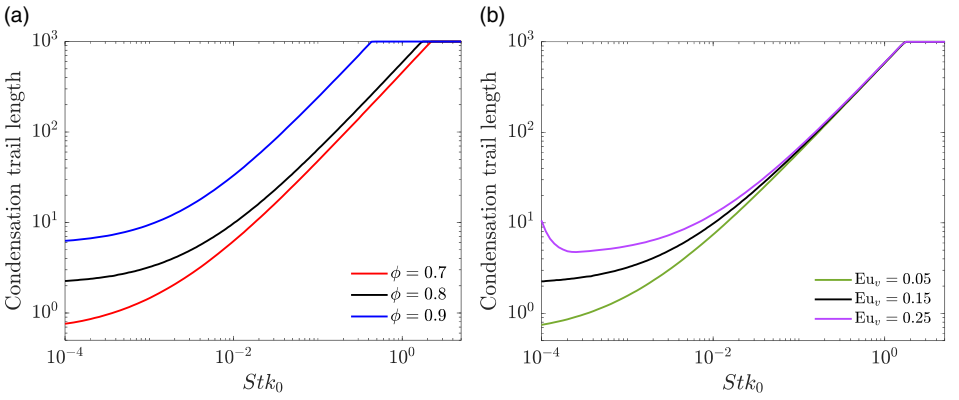

Figure 7. *Comparison of condensation trail length normalised by the chord length, as a function of the initial droplet Stokes number* Stk_0 *at different thermodynamic and flow conditions. (a) Effects of changes in the air relative humidity* ϕ*. (b) Effects of changes in the vortex Euler number* Eu_v*.*

4.0 Conclusions

A mathematical analysis of discrete droplet dynamics within a Batchelor vortex was conducted, revealing the complex coupling between the droplet motion and the thermodynamic gradients generated by the vortex. A Lagrangian approach is used to analyse the coupling between droplet motion and the flow field generated by the vortex. Under certain thermodynamic and hydrodynamic conditions, droplets may undergo evaporation and condensation when circulating the vortex core due to sharp changes in the environmental conditions induced by the vortex. We evaluated the pressure drop due to the vortical flow, quantifying it using a non-dimensional vortex Euler number Eu_v. The resultant gradients may be large enough to initiate condensation within the vortex core. The onset of condensation was studied by defining a mass transfer coefficient C_m, indicating the direction and extent of mass transfer to the Lagrangian water droplet. Our study uncovered a distinct clustering phenomenon linked to the initial Stokes number, with droplets showing a tendency to aggregate at higher Stokes numbers. In summary, the presented model offers valuable insights into droplet dynamics within trailing vortices, contributing to improved modelling and prediction of droplet transport phenomena across various fields, from atmospheric science to engineering applications.

Funding statements. This research was supported by the ISRAEL SCIENCE FOUNDATION (grant No. 1762/20).

References

[1] Pullin, D.I. and Saffman, P.G. Vortex dynamics in turbulence, *Annu. Rev. Fluid Mech.,* 1998, **30**, 31.
[2] Dávila, J. and Hunt, J.C. Settling of small particles near vortices and in turbulence, *J. Fluid Mech.,* 2001, **440**, 117.
[3] Chakroun, N.W., Shanbhogue, S.J., Dagan, Y. and Ghoniem, A.F. Flamelet structure in turbulent premixed swirling oxy-combustion of methane, *Proc. Combust. Inst.,* 2019, **37**, 4579.
[4] Dagan, Y., Katoshevski, D. and Greenberg, J.B. Similarity solutions for the evolution of unsteady spray diffusion flames in vortex flows, *Combust. Sci. Technol.,* 2018, **190**, 1110.
[5] Dagan, Y., Arad, E. and Tambour, Y. The evolution of local instability regions in turbulent non-premixed flames, *J. Fluid Mech.,* 2016, **803**, 18.
[6] Taamallah, S., Dagan, Y., Chakroun, N., Shanbhogue, S.J., Vogiatzaki, K. and Ghoniem, A.F. Helical vortex core dynamics and flame interaction in turbulent premixed swirl combustion: A combined experimental and large eddy simulation investigation, *Phys. Fluids,* 2019, **31**, 25108.
[7] Dagan, Y., Chakroun, N.W., Shanbhogue, S.J. and Ghoniem, A.F. Role of intermediate temperature kinetics and radical transport in the prediction of leading edge structure of turbulent lean premixed flames, *Combust. Flame,* 2019, **207**, 368.
[8] Dagan, Y., Arad, E. and Tambour, Y. On the dynamics of spray flames in turbulent flows, *Proc. Combust. Inst.,* 2015 **35**, 1657.
[9] Dagan, Y. Settling of particles in the vicinity of vortex flows, *At. Sprays*, 2021, **31**, 33.

https://doi.org/10.1017/aer.2025.45 Published online by Cambridge University Press

[10] Avni, O. and Dagan, Y. Dynamics of evaporating respiratory droplets in the vicinity of vortex dipoles, *Int. J. Multiph. Flow,* 2022, **148**, 103901.
[11] Avni, O. and Dagan, Y. Dispersion of free-falling saliva droplets by two-dimensional vortical flows, *Theor. Comput. Fluid Dyn.,* 2022, **36**, 993.
[12] Avni, O. and Dagan, Y. Droplet dynamics in burgers vortices. i. mass transport, *Phy. Rev. Fluids,* 2023, **8**, 083604.
[13] Avni, O. and Dagan, Y. Droplet dynamics in burgers vortices. ii. heat transfer, *Phys. Rev. Fluids,* 2023, **8**, 083605.
[14] Jugier, R., Fontane, J., Joly, L. and Brancher, P. Linear two-dimensional stability of a lamb-oseen dipole as an aircraft wake model, *Phy. Rev. Fluids,* 2020, **5**, 014701.
[15] Atias, M. and Weihs, D. On the motion of spray drops in the wake of an agricultural aircraft, *At. Sprays,* 1985, **1**, 21.
[16] Sölch, I. and Kärcher, B. A large-eddy model for cirrus clouds with explicit aerosol and ice microphysics and lagrangian ice particle tracking, *Q. J. R. Meteorol. Soc.,* 2010, **136**, 2074.
[17] Unterstrasser, S. and Sölch, I. Study of contrail microphysics in the vortex phase with a lagrangian particle tracking model, *Atmos. Chem. Phys.,* 2010, **10**, 10003.
[18] Holzäpfel, F., Stephan, A., Heel, T. and Körner, S. Enhanced wake vortex decay in ground proximity triggered by plate lines, *Aircraft Eng. Aerospace Technol.,* 2016, **88**, 206.
[19] Campbell, J.F. and Chambers, J.R., Patterns in the sky: Natural visualization of aircraft flow fields, in NASA-SP-514 (1994).
[20] Batchelor, G.K. Axial flow in trailing line vortices, *J. Fluid Mech.,* 1964, **20**, 645.
[21] Saffman, P.G. *Vortex Dynamics*, Cambridge University Press, 1993.
[22] Maxey, M.R. and Riley, J.J. Equation of motion for a small rigid sphere in a nonuniform flow, *Phys. Fluids,* 1983, **26**, 883.
[23] Crowe, C.T., Schwarzkopf, J.D., Sommerfeld, M. and Tsuji, Y. 2nd ed., CRC Press, 2011, Boca Raton.
[24] Kulmala, M., Majerowicz, A. and Wagner, P.E. Condensational growth at large vapour concentration: Limits of applicability of the mason equation, *J. Aerosol Sci.,* 1989, **20**, 1023.
[25] Kulmala, M. and Vesala, T. Condensation in the continuum regime, *J. Aerosol Sci.,* 1991, **22**, 337.

Cite this article: Avni O. and Dagan Y. Phase-changing droplet dynamics in idealised trailing vortex flows. *The Aeronautical Journal*, https://doi.org/10.1017/aer.2025.45